Journal of Structural Geology, Vol. 14, No. 3, pp. 257 to 269, 1992
Printed in Great Britain

0191-8141/92 $05.00+0.00

Perturbations of strain and rotation in a nodular slate

G. OERTEL

Department of Earth and Space Sciences, University of California, Los Angeles, CA 90024, U.S.A.

and

A. P. S. REYMER

Department of Marine, Earth and Atmospheric Sciences, North Carolina State University, Raleigh, NC 27695, U.S.A.

(*Received* 23 *October* 1990; *accepted in revised form* 23 *July* 1991)

Abstract—Strain is estimated at the hinge and in one limb of an anticline by the measurement of phyllosilicate preferred orientation in the matrix of a nodular, calcareous slate at three-dimensional grid points. We calculate an average strain for each and also the average shapes of the calcite-cemented nodules, which we explain by a strain distinct from that of the matrix acting on originally oblate spheroidal concretions.

Cleavage folia show symptoms of stress solution, and the nodular concretions are capped by strain shadows almost free of cleavage; the nodules were stiffer than the matrix during most of the deformation history. Near the concretions the strain is too inhomogeneous at a small scale to allow the resolution of details of the strain field.

The local strain we take to be the compound of the average and a perturbing strain. The strain perturbations are not random but statistically share their intermediate principal axis; these axes are less tightly clustered in the hinge than in the limb. The axes of local rotations that are concomitant with the perturbing strains also have only a slight preferred orientation in the hinge, but they are statistically aligned in the limb. There, all axes lie near the cleavage great circle, and they cluster near the fold axis. The regularity of the rotation axes indicates a history of simple, flexural shear in the limb, with the local rotations caused by retardations or accelerations of the shear rate near stiff nodules.

Comparisons between the mean strain in hinge and limb, strained nodule shapes, strain perturbations and perturbing rotations allow recognition of several distinct episodes of strain: (1) 40% compaction; (2) 9% homogeneous bedding-parallel contraction; (3) buckling; and (4) a further 33% bedding-parallel contraction in the hinge and 37% approximately bedding-normal contraction in the limb. Volume loss was greatest near the concretions, both during compaction and later by stress solution; the limb lost 13% more volume than the hinge.

INTRODUCTION

THE original goal of this research was to investigate in detail the effects of stiff nodules on the strain field caused by folding a nodular slate. The attempt was unsuccessful: the minimum sample size needed for X-ray measurements of the preferred orientation of phyllosilicates, to be used for strain determinations according to March (1932), turned out to be too large to resolve the relevant details. The work did, however, furnish two relatively large measurement sets of preferred orientations, one from the hinge and one from the limb of the fold, and statistical investigation of these data revealed that, even without knowledge of how each concretion affected the strain field, conclusions could be drawn about the kinematics of folding.

In any heterogeneous strain field, continuity requires locally varying rigid-body rotations between the initial and final states. Domains must rotate relative to their neighbors and, except perhaps for a fortuitous few, relative to a reference frame, even if on the whole the heterogeneously strained body should not rotate with respect to that frame. Our two sets of measurements thus allow calculation of the rotations of constituent subdomains with respect to the reference frame provided by the specimen domain as a whole, and that is one of the objects of this paper. The overall rigid-body rotation of the specimen domain, on the other hand, leaves no physical traces except for its effect on the bedding attitude, evidence which by itself is insufficient for complete reconstruction because the effects of potential rotations about an axis parallel to the bedding pole cannot be observed.

In northwest England several inliers of folded early Paleozoic strata are surrounded by outcrops of nearly horizontal Carboniferous sediments. The Horton-in-Ribblesdale inlier, north of Stainforth, Yorkshire, exposes Wenlock and Lower Ludlow rocks (McCabe 1972, McCabe & Waugh 1973). Silty slates, some rich in calcite-cemented concretions, in the Sunny Bank quarry west of the river Ribble near Helwith Bridge belong to the informally named Horton Flags, which comprise the top of the Wenlockian Arcow and bottom of the Lower Ludlovian Horton Formations and are approximately 400 m thick. They are both over- and underlain by thick sequences of graywackes with minor mudstones. The outcrop of Horton Flags studied in this paper lies in the southern limb of an E-plunging synclinorium (McCabe & Waugh 1973) and, before the lower quarry level was allowed to fill with water, the western face showed the hinge and northern limb of an anticline (Fig. 1). The fold axis, as defined by a single, whaleback-shaped bedding surface, steepens eastward.

Almost homogeneous calcareous slates, 80 m thick

stratigraphically, are exposed in the quarry, the main distinction from bed to bed being the presence in some of closely spaced calcite-cemented nodules. No single nodular layer could be followed from the hinge to the steep portion of the limb, and two different beds were sampled (Fig. 1). The fold axis trends 100–110° throughout the quarry, but along a 150 m long curved line its plunge steepens from 15° at the upper level to 35° at the quarry floor. The limb sample thus belongs to a less steeply plunging portion of the fold than the hinge sample, and the line of intersection of the bedding planes at the two localities, or geometric fold axis, which happens to trend 90° and to plunge 35° (Fig. 2), has no kinematic significance. Cleavage strikes between 100° and 110° and forms an inverted fan from vertical at the hinge to decreasingly steep southward dips in the limb until, as the cleavage orientation approaches that of the bedding, the two become indistinguishable in the field.

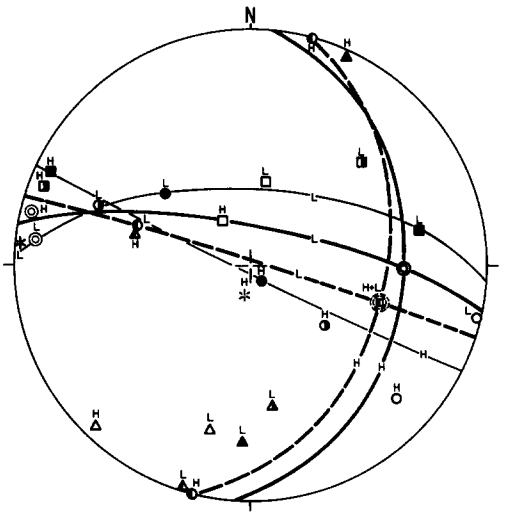

Fig. 2. Equal-area projection of mean principal strain axes and foliations. Lower-hemisphere. Squares—maximum axes (extension). Circles—intermediate axes. Triangles—least axes (shortening). Full squares, etc.—axes of mean strain. Open squares, etc., axes of mean nodule shape. Squares, etc., filled on the left—axes of 'early' strain. Squares, etc., filled on the right—axes of 'late' strain. Light double circles—mean intermediate axes of strain perturbations. Asterisks—axes of mean perturbing rotation. Heavy great circles—bedding. Dashed heavy great circles—bedding unstrained. Light great circles—cleavage. H—hinge. L—limb. Heavy double circle—geometric fold axis. Heavy dashed double circle—kinematic fold axis.

TEXTURES

Figure 3 shows a thin section from the hinge viewed toward the east. The fold axis forms an angle of 65° with the section. The apex of a nodule, which has a vertical longest axis, appears at the bottom left (Fig. 3a). Similar detrital grains, mostly phyllosilicates, dominantly chlorite and some quartz, are observed in the same calcite cement in both matrix and nodule, but the clasts are more widely spaced in the nodule. Cleavage, as expressed by folia rich in phyllosilicates, wraps around the nodule and an almost cleavage-free strain shadow that extends obliquely upward from the apex. Cleavage folia are densest at the northern nodule contact; upward along the boundary with the strain shadow the dense region continues but fades. The N–S asymmetry of folia density is common at other nodules but without a systematic preference for the northern contact. In detail, Fig. 3(b) shows the boundary folium typically thicker than most others. Although some folia split or rejoin, they are discontinuous, and their traces do not combine into an anastomosing network; they form a similar pattern at some distance south of the nodule (Figs. 3c & d), where the cleavage is not noticeably influenced by the vicinity of the nodule. There are no indications of grain overgrowth or crystal plasticity.

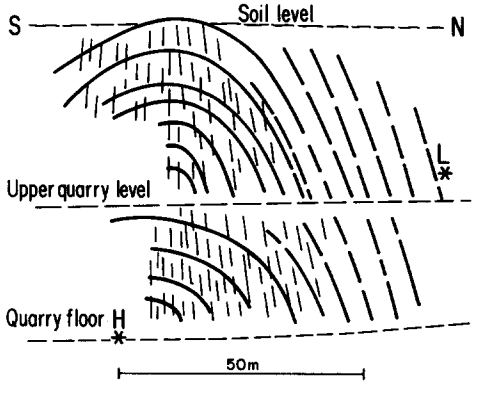

Fig. 1. West wall of Sunny Bank quarry near Helwith Bridge, Yorkshire, U.K. View to the west from the hinge sampling point. In the hinge, midway between soil and upper quarry level, the fold axis plunges 15° toward the viewer, at the quarry floor it plunges 35°. L—limb sampling point. H—westward projection of hinge sampling point. The blank region is occupied by a single exposed bedding surface, which along the hinge slopes east toward the viewer with an increasing dip and bends to a northerly dip north of the hinge line.

Figure 4 shows a nodule in the limb in approximately downward view, cut so as to show the intermediate and short axes. Cleavage and bedding (trace evident near the top of the photograph) approximately parallel the two longer nodule axes. The contrast between nodule and matrix is sharp where cleavage folia are dense (above the nodule, detail in Fig. 4b) but inconspicuous in the strain shadow to the left of the nodule; there the matrix is almost unaffected by cleavage, and the proportion of former pore space now filled with calcite is hardly less than in the nodule itself. Although the cement in the strain shadow is necessarily younger than that in the nodule, both regions must eventually have had nearly identical mechanical properties, as indicated by the smooth passage of a calcite-filled tension gash through both. The angle between bedding and cleavage being small, lithological contrast between beds causes an especially thick boundary folium on the slaty side (Fig. 4c), much in the same way as it does along nodules. Neither overgrowth nor crystal plasticity can be documented.

NODULE SHAPES

The shapes of most concretions approach an ellipsoid (representative saw cut faces are shown in Fig. 5), and only a few of them are stratiform (Fig. 5c). An average

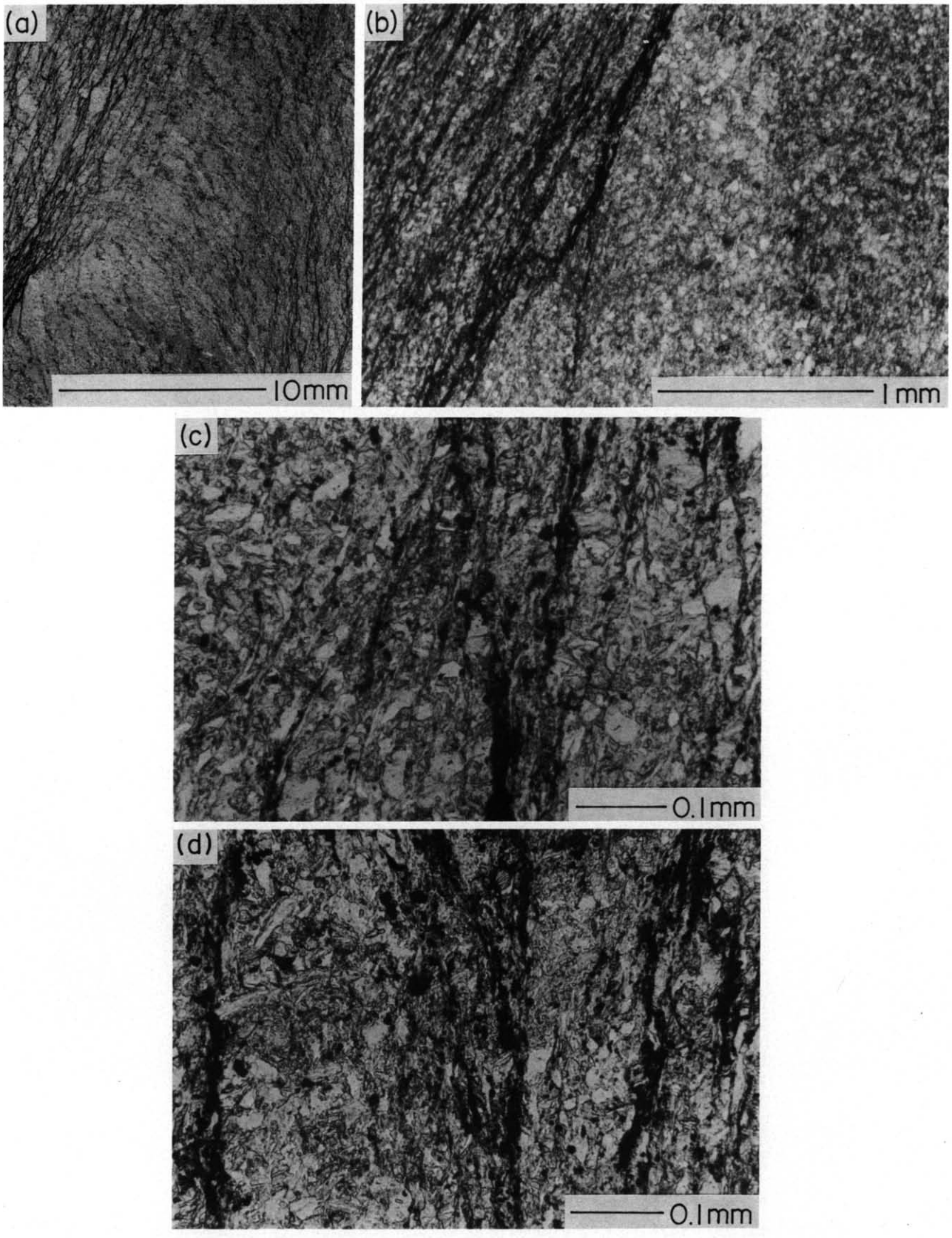

Fig. 3. Thin section from the fold hinge region. Section plane vertical and orthogonal to cleavage and fold-axis trend; view horizontally eastward. (a) Whole section. (b) Nodule–matrix contact. (c) & (d) Details of cleavage.

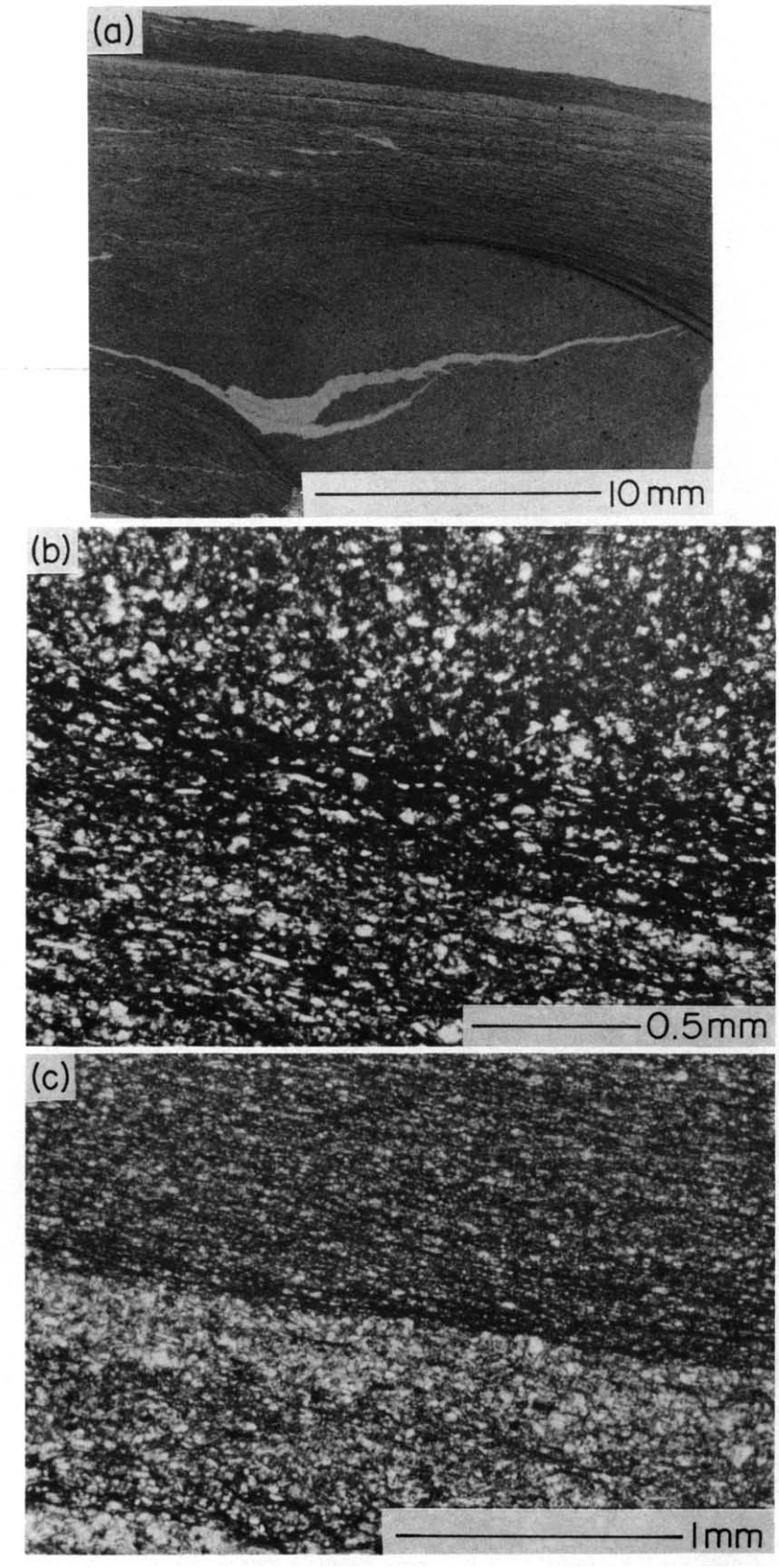

Fig. 4. Thin section from limb region. Oblique downward view onto a 27° S-dipping plane; top edge of photograph (North) is horizontal and strikes 95°. Cleavage perpendicular to the section. (a) Whole section. (b) Nodule contact with cleaved matrix. (c) Bedded matrix.

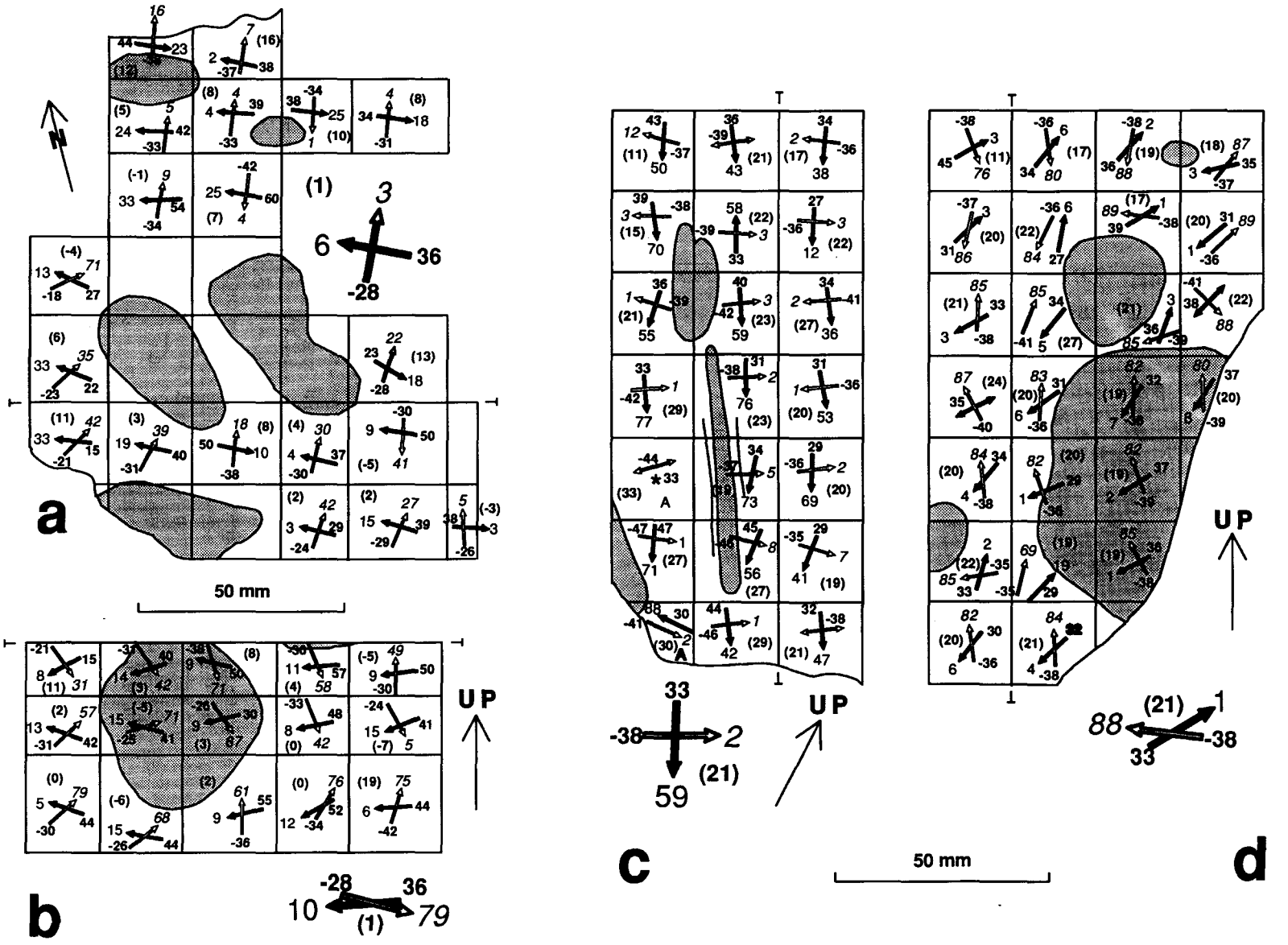

Fig. 5. Selected sections through (a & b) hinge and (c & d) limb. (a) Downward view of horizontal face. Strain symbols refer to subsamples below the face. (b) Approximately northward view, along fold axis trend, of vertical, 105°-striking face. Strain symbols refer to subsamples in front (south) of the face. (c) Approximately eastward view of vertical, 5°-striking face. Strain symbols refer to subsamples behind (east of) the face. (d) Oblique, approximately south- and downward view onto 95°-striking and 63° N-dipping face. Strain symbols refer to subsamples behind (south of) the face and behind the concretion. All sections: Straight, thin lines—saw cuts orthogonal to sections. |– –|—trace of illustrated orthogonal face. Shaded—concretion. Black arrows—projections of largest principal strain direction; number at head—angle with face; bold number at tail—magnitude (in percent, normalized to constancy of volume). Hollow arrows—projections of least principal strain direction; italic number at head—angle with face; bold number at tail—magnitude. Double-headed arrows—principal direction parallel to face. Asterisk—principal direction orthogonal to face. Bold numbers in parentheses—magnitudes of intermediate principal strain (direction orthogonal to those of largest and least). A—axially symmetric strain. Large strain symbols—sample-means for hinge or limb, respectively.

Table 1. Strain in the hinge

Sample	[Principal strains]			(Trends and plunges)		
H 1	[0.27	−0.04	−0.18]	(310, 13)	(216, 14)	(81, 71)
H 2	[0.22	0.06	−0.23]	(306, 33)	(186, 37)	(63, 35)
H 3	[0.15	0.11	−0.21]	(294, 33)	(182, 30)	(60, 42)
.						
.				(Complete list available on request)		
.						
H 58	[0.52	0.12	−0.41]	(303, 29)	(85, 55)	(202, 18)
H 59	[0.44	0.19	−0.42]	(291, 5)	(35, 71)	(199, 18)
H 60	[0.55	0.07	−0.40]	(297, 13)	(54, 63)	(202, 23)
Mean	[0.36	0.01	−0.28]	(295, 6)	(143, 84)	(25, 3)
Vol. loss	[0.15	−0.14	−0.39]	(295, 6)	(143, 84)	(25, 3)
Early	[0.00	−0.09	−0.34]	(105, 42)	(195, 0)	(285, 48)
Late	[1.54	−0.12	−0.55]	(292, 30)	(128, 59)	(26, 7)
Nodule	[1.28	1.13	0.69]	(329, 72)	(132, 17)	(224, 5)
Bedding pole, observed					(275, 55)	
Bedding pole, unstrained					(284, 48)	
Cleavage pole, mesoscopic						(20, 0)
Kinematic fold axis				(105, 42)		
Mean axis of rotations due to perturbations				(193, 80)		

shape for hinge and limb of all but the obviously stratiform nodules was estimated by statistically combining average ellipses calculated from observations on each set of parallel faces. The estimation method of Oertel (1978) and Miller & Oertel (1979) was modified to accommodate the large variances of observed shapes. Averages and errors, instead of being calculated from the ellipse axes themselves, were derived from their natural logarithms, combined into two-dimensional tensors which are referred to a common co-ordinate system. These plane logarithmic tensors were combined into three-dimensional tensors, and the exponentials of their eigenvalues were taken to be the axes of the mean shape ellipsoids. This procedure avoids some of the difficulties (see Oertel 1981, Wheeler 1986) that follow from the non-linear properties of finite strain.

The mean principal radii of nodules in the hinge (Fig. 2) are [1.28, 1.13, 0.69] ± 0.12 (the stated uncertainty is the root-mean-square of the several estimated standard deviations of the shape-tensor components) with the long axis near the dip-line of bedding and the short axis near the cleavage pole. We may assume that the original nodules had, on average, the shape of an oblate spheroid with its short axis normal to bedding, as is commonly observed in sediments undeformed except for some compaction of the matrix (although the degree of original deviation of nodule shape from sphericity varies). If this assumption is correct, tectonic stretching must have converted the short original nodule radius into what is now one of the longest material lines.

In the limb, the mean nodule (Fig. 2) has axes [1.37, 1.26, 0.58] ± 0.06 with the long axis almost exactly down-dip on the cleavage and the intermediate axis along its strike. Because the attitudes of cleavage and bedding differ so little, the short axis lies near the poles of both. The modification of the average nodule shape from a presumable bedding-parallel oblate spheroid to its present triaxial shape appears less radical than in the hinge.

STRAIN ESTIMATES FROM PHYLLOSILICATE ORIENTATIONS

The oriented samples were cubed by saw cuts to yield subsamples (Fig. 5). From two orthogonal sides of each subsample at the largest angles with the cleavage, wafers were sliced for thick sections that could be mounted on an X-ray pole-figure goniometer specially adapted for transmitted-mode measurements of preferred orientation (Oertel 1985a, Wenk 1985). The dominant phyllosilicate mineral is chlorite, and its preferred orientation patterns were interpreted as indicators of cumulative strain since deposition (Oertel 1985b) according to the method of March (1932) who first treated tabular grains in a rock as quantitative strain markers. This strain is customarily stated in normalized form, as if there had been no volume change, because even complete knowledge of preferred orientation leaves the volume change indeterminate.

Orientations of the principal strain axes in hinge and limb are scattered, and so are the principal values (examples in Tables 1 and 2, complete strain lists available from G. Oertel on request), but they are far from random. In the hinge (Fig. 6a), maximum axes are clustered in the horizontal ESE direction and the intermediate and least axes are spread along a great circle. On that great circle, the least axes are clustered near the horizontal, but the spreads of the intermediate and least axes overlap. In the limb (Fig. 6d), it is the least axes that are most clustered; they plunge to the south while the intermediate and maximum axes are spread in a great-

Table 2. Strain in the limb

Sample	[Principal strains]			(Trends and plunges)		
L 1	[0.32	0.19	−0.36]	(293, 8)	(29, 40)	(194, 49)
L 2	[0.40	0.17	−0.39]	(71, 39)	(298, 40)	(184, 26)
L 3	[0.45	0.11	−0.38]	(78, 24)	(326, 40)	(191, 40)
.						
.				(Complete list available on request)		
.						
L 71	[0.47	0.25	−0.46]	(87, 30)	(294, 57)	(184, 12)
L 72	[0.43	0.20	−0.42]	(78, 45)	(290, 40)	(185, 17)
L 73	[0.37	0.20	−0.39]	(70, 54)	(286, 30)	(185, 17)
Mean	[0.33	0.21	−0.38]	(78, 27)	(311, 50)	(183, 27)
Vol. loss	[0.03	−0.06	−0.52]	(78, 27)	(311, 50)	(183, 27)
Early	[0.00	−0.09	−0.34]	(105, 42)	(289, 48)	(197, 2)
Late	[0.19	0.04	−0.37]	(45, 32)	(292, 31)	(169, 42)
Nodule	[1.37	1.26	0.58]	(10, 60)	(102, 1)	(193, 30)
Bedding pole, observed						(190, 14)
Bedding pole, unstrained						(197, 2)
Cleavage pole, calculated						(183, 27)
Kinematic fold axis				(105, 42)		
Mean axis of rotations due to perturbations				(276, 2)		

circle zone; in that zone, the maximum axes cluster somewhat around an E-plunging line, the intermediate axes about a steeply NW-plunging line.

FACTORIZATION INTO SPECIMEN MEAN AND PERTURBATION STRAINS

A mean logarithmic strain (at nominal constant volume) was calculated for both hinge and limb according to the method described by Oertel (1981); briefly, averages for populations of corresponding components of individual logarithmic strains are taken to be the components of a mean logarithmic strain tensor, and the exponentials of that tensor's eigenvalues, together with the eigendirections, yield the mean strain. The mean strain in the hinge is [0.36, 0.01, −0.28] ± 0.01, a plane strain with the maximum near the trend line of the fold axis; the least strain is also nearly horizontal (Figs. 2 and 6a). The mean strain in the limb, on the other hand, is [0.33, 0.21, −0.38] ± 0.01 and thus lies in the flattening range; the maximum plunges eastward, not far from the direction of the fold axis, the lesser elongation steeply northwestward, and the least strain and cleavage pole gently southward (Figs. 2 and 6d).

Bedding attitude can be restored to its hypothetical pre-mean-strain orientation (see Appendix), by eliminating the effect of the strain but not the rigid-body rotation a domain may have suffered at any stage, before, during, or after the strain. Assuming arbitrarily that the rotation came first, we find that before the strain, bedding in the hinge had a strike of 14° rather than 5° and it dipped more steeply, 42° E; unstraining the limb modifies bedding strike from 100° to 107° and steepens it to 88° N (Fig. 2). The angle of 87° between the unstrained bedding attitudes in hinge and limb represents the rigid-body rotation that would have been caused by buckling the stiffest beds in the stack. If, in fact, much of the rotation had occurred early (although probably after compaction, which does not affect bedding attitudes), then the intersection of these two planes would represent the fold axis at the onset of buckling, and it may therefore be called the kinematic fold axis. Within the margin of error, it lies on the cleavage plane, and it trends 105°, plunges 42°, and differs significantly from the geometric fold axis defined by the intersection of the present bedding planes (Fig. 2).

It is conceptually convenient to decompose the observed strain into the specimen mean strain and a local excess strain, called a 'perturbation', taken arbitrarily to have preceded the mean strain. These local perturbations were most probably physically caused by the stiffness contrast between nodules and matrix (Fig. 5), and they can be mathematically separated by strain factoring (see Appendix). For the calculation, the mean strain must be eliminated from the observed strain. This can be achieved by taking each perturbation to be the effect of an imaginary sequence of two, generally noncoaxial, finite strain increments, the locally measured strain followed by the inverse of the sample-mean strain. The resulting perturbation is necessarily the compound of a rigid-body rotation and an irrotational strain. For ease of representation, one usually expresses such a transformation as the sequence of rotation and irrotational strain or polar decomposition (without the implication that the two really occurred sequentially). In order to have the strain perturbation, the part of the transformation that is likely to leave physical evidence in the rock, referred to co-ordinates in the specimen, we decomposed the transformation as if it had consisted of the perturbing rotation first and the irrotational perturbing strain last (left-polar). Tables 3 and 4 contain examples of principal values and directions of the perturbing strains and of the angles and axes of rotation (complete perturbation lists are available from G. Oertel on request), and the principal directions and rotation axes are shown synoptically in Figs. 6(b) & (e).

Although, for each sample, the tensor sum of the

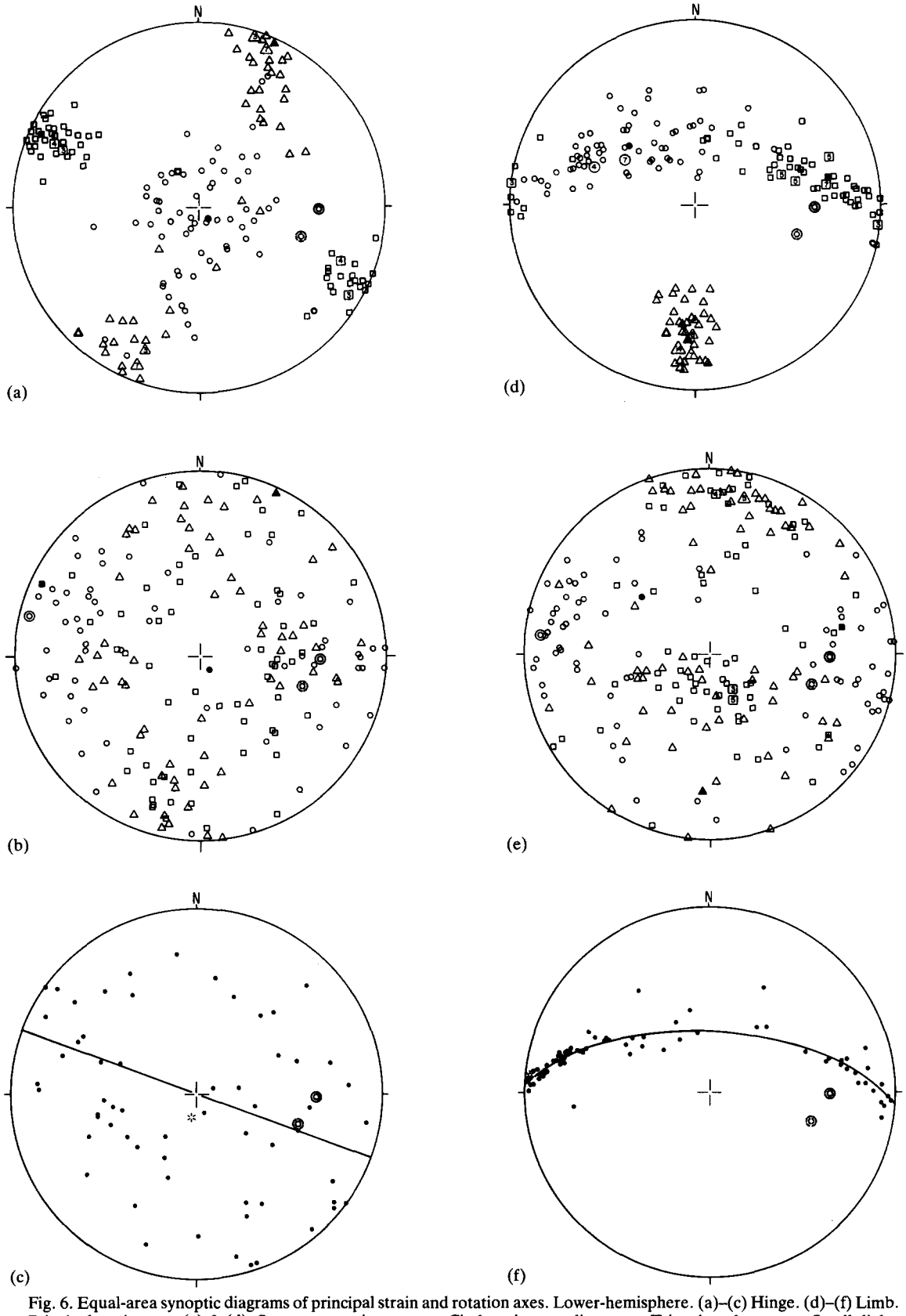

Fig. 6. Equal-area synoptic diagrams of principal strain and rotation axes. Lower-hemisphere. (a)–(c) Hinge. (d)–(f) Limb. Principal strain axes, (a) & (d). Squares—maximum axes. Circles—intermediate axes. Triangles—least axes. Small, light, open squares, etc.—axes from individual measurements. Large, light, open squares, etc.—axes from multiple measurements (number inserted). Full squares, etc.—mean principal axes. Heavy open square, etc.—principal axes of mean nodule shapes. Heavy double circle—geometric fold axis. Dashed heavy double circle—kinematic fold axis. Principal axes of strain perturbations, (b) & (e). Squares—maximum axes. Circles—intermediate axes. Triangles—least axes. Small, open squares, etc.—axes of individual strain perturbations. Large, open squares, etc.—axes of multiple strain perturbations (number inserted). Light double circle—mean intermediate axis of strain perturbations. Full square, etc.—axes of mean strain. Heavy double circle—geometric fold axis. Dashed heavy double circle—kinematic fold axis. Axes of perturbing rotation, (c) & (f). Dots—individual axes. Asterisk—mean axis. Great circle—cleavage. Double circle—geometric fold axis. Dashed double circle—kinematic fold axis.

logarithmic strain perturbations and the vector sum of the perturbing rotations must be zero by definition, their orientation distributions are not necessarily random. Since the strain perturbations are local departures from the average strain, the perturbing rotations represent the concurrent rigid-body adjustments enforced by the need for spatial continuity from one subdomain to the next.

The only apparent regularity in the orientation of perturbation strain axes in the hinge (Fig. 6b) is a concentration of intermediate axes in a wide region surrounding a line trending 284° and plunging 6° with a corresponding scarcity of the same axes in a vertical N–S zone. Within this zone, the maximum and least strain-perturbation axes predominate but are not separated from each other. Perturbing rotations are generally small (the arithmetic mean of absolute rotations is 1.7°), their axial orientations (Fig. 6c) depart only slightly from random, and the vector mean of the absolute (sense disregarded to avoid cancellation) rotations is nearly vertical and only 0.6 times as large as the arithmetic mean (the higher the ratio of vector to arithmetic mean, the sharper is the alignment of the rotation axes).

Strain perturbation axes in the limb (Fig. 6e) are more regular than those in the hinge. The intermediate axes are clustered about a line that trends 277° and plunges 8°, almost parallel to the corresponding hinge cluster. If no distinction is made between axes of greatest perturbing shortening and stretching, these strain axes form two clusters, one plunging steeply to the south and the other gently to the NNE. Perturbing rotations are larger, on average, than in the hinge (the arithmetic mean of absolute rotations is 2.4°), and the axes (Fig. 6f) lie in a narrow zone on either side of the cleavage great-circle. In this zone they form a pronounced cluster about the vector mean of absolute rotations trending 276° and plunging 2°. The magnitude of that mean is 1.8 times the arithmetic mean.

DISCUSSION

Textures

The cleavage folia appear to be solution seams. All the calcareous cement and most of the silt-size quartz present in the intra-folial lithons are missing. Unless there are unobservable overgrowths on clastic or cement grains, much of the dissolved material must have been carried away, calcite-filled cracks (Fig. 4a) being few and of insignificant volume. The folia may be considered anticracks (Fletcher & Pollard 1981) which, like ordinary cracks, usually require a critical threshold stress to cause the instability necessary for initiation or growth. The sharp boundaries between strain shadows and cleaved regions in the matrix are further evidence for a threshold stress needed to initiate and maintain dissolution. Cleavage folia are absent, or small and rare, in these strain shadows, which cap concretions at boundaries facing into the directions of least contraction. The shadows are proof of a stiffness contrast between concretions and matrix during a large part of the strain history.

Nodule shapes

In the beginning, the nodules were stiffer than the matrix and protected their vicinity from compaction, as documented by the undiminished calcite-filled pore space in the strain shadows (Figs. 3 and 4). As the matrix was consolidated, and perhaps with increasing temperature, the stiffness contrast between matrix and nodules decreased, and the nodules began to participate in the strain. Without exact knowledge of the original concretion shapes, strain in the nodules can only be guessed; it did, however, differ markedly from that in the matrix. The nodules in both hinge and limb were most stretched in a steeply northward-plunging direction (Fig. 2).

Table 3. Strain perturbations in the hinge

Sample	[Principal strains]	(Trends and plunges)			Rotation	(Trend, plunge)
H 1	[0.36 −0.08 −0.20]	(14, 2)	(283, 33)	(107, 57)	−1.5	(217, 67)
H 2	[0.35 0.04 −0.29]	(193, 12)	(306, 62)	(98, 26)	−2.7	(239, 54)
H 3	[0.41 −0.04 −0.26]	(198, 16)	(318, 60)	(100, 25)	−2.1	(259, 44)
.						
.		(Complete list available on request)				
.						
H 58	[0.32 0.00 −0.25]	(345, 55)	(94, 13)	(192, 32)	−2.5	(139, 5)
H 59	[0.27 0.06 −0.26]	(47, 55)	(291, 17)	(191, 29)	2.6	(297, 31)
H 60	[0.22 0.10 −0.26]	(347, 47)	(94, 15)	(196, 40)	−2.3	(125, 0)
Mean	[0.36 0.01 −0.28]	(295, 6)	(143, 84)	(25, 3)		
Arithmetic mean of absolute rotations					1.7	
Vector mean of absolute rotations					1.0	(193, 80)
Bedding pole, observed			(275, 55)			
Bedding pole, unstrained			(284, 48)			
Cleavage pole, mesoscopic				(20, 0)		
Kinematic fold axis		(105, 42)				
Mean axis of intermediate strain perturbation			(284, 6)			

Table 4. Strain perturbations in the hinge

Sample	[Principal strains]	(Trends and plunges)	Rotation	(Trend, plunge)
L 1	[0.36 −0.04 −0.24]	(345, 5) (75, 6) (214, 82)	4.7	(86, 20)
L 2	[0.06 −0.02 −0.04]	(71, 54) (178, 12) (275, 34)	0.3	(325, 33)
L 3	[0.15 0.08 −0.20]	(8, 9) (101, 20) (255, 68)	2.8	(86, 16)
.				
.		(Complete list available on request)		
.				
L 71	[0.23 0.07 −0.24]	(128, 69) (271, 17) (5, 12)	4.5	(278, 11)
L 72	[0.20 −0.02 −0.15]	(124, 68) (273, 19) (7, 10)	3.2	(284, 17)
L 73	[0.18 −0.05 −0.11]	(148, 72) (285, 13) (18, 12)	2.8	(284, 16)
Mean	[0.33 0.21 −0.38]	(78, 27) (311, 50) (183, 27)		
Arithmetic mean of absolute rotations			2.4	
Vector mean of absolute rotations			4.2	(276, 2)
Bedding pole, observed		(190, 14)		
Bedding pole, unstrained		(197, 2)		
Cleavage pole, calculated		(183, 27)		
Kinematic fold axis		(105, 42)		
Mean axis of intermediate strain perturbation		(278, 8)		

Strain in the matrix and possible volume changes

The preferred orientation of tabular mineral grains provides no information about volume changes, yet such changes are important for physical interpretations and must in our case have been large during compaction and still significant during cleavage formation by stress solution. For an estimate of volume loss we depend on conjecture.

Volume loss can be calculated if material lines parallel to the fold axis have maintained their original length (Oertel *et al.* 1989). For cylindrical folds this assumption is unexceptional, but the material lines along the curved axis of our fold may have been stretched over an axial culmination in the hypothetical, unexposed, competent layer at depth that caused the cleavage fan. Discounting such an effect as insignificant, total volume loss (by both compaction and tectonic stress solution) can be calculated as 40% in the hinge, 53% in the limb. Differential volume loss is plausible; after a common compaction, the hinge may have lost much less by solution than the limb. Mean principal strain values, modified from the normalized values to fit this assumption, are shown in Tables 1 and 2.

Accepting as most plausible the hypothesis of approximate conservation of length along the fold axis allows further conclusions. For the sake of a definite statement, all the volume loss in the hinge is taken to have been due to compaction. If both hinge and limb had lost 40% of their volume before buckling, then another 13% loss of original volume, or 22% of compacted volume, would have brought the volume in the limb to its present state. Compaction of 40% (or even less if some of the lost volume of the hinge is ascribed to tectonically caused solution) may be low for an uncemented silty mudstone (Bond & Kominz 1984) but is plausible for the calcite-cemented Horton Flags; even incipient cementation slows compaction by clogging the passages needed for fluid expulsion. The maximum-strain direction in the hinge nearly parallels the fold axis and is thus, according to our assumption, a line of insignificant strain; setting it to zero and making the necessary correction for volume loss yields a negative intermediate principal strain of −0.09. This is compatible with an episode of pre-buckling, bedding-parallel contraction at constant volume (Chapple 1969), which would have affected hinge and limb regions uniformly.

The common history of hinge and limb, by this most-plausible hypothesis, consists of 40% compaction and a pre-buckling tectonic strain. The first two axes of this common 'early strain' of [−0.09, 0, −0.34] lie in the horizontal bedding plane, the second being parallel to the future fold axis, and the third is vertical. The original compaction of −0.40 is reduced to a vertical shortening of only −0.34 by tectonic elongation at constant volume. Bedding, lying in a principal plane, did not change attitude during this early strain.

The separate histories of hinge and limb began with rigid-body rotations, caused by entrainment between buckling, less ductile layers below and above. Either before, along with, or after the rotations that brought the fold axis to its various present orientations, the limb rotated with respect to the hinge about the kinematic fold axis. The 'late strain' that either followed these rotations or was concurrent with them conserved volume in the hinge (by assumption) but induced a 22% volume loss in the limb. The late strain factor in the hinge, calculated by removing the earlier factor, is [0.59, −0.06, −0.33], essentially a plane strain but slightly constrictional; its long axis plunges gently to the west, the intermediate steeply to the southeast, and the least is near-horizontal with a NNE trend (Fig. 2 and Table 1). The 'late strain' in the limb is [0.19, 0.04, −0.37], thus nearly plane but slightly flattening; its long axis plunges gently northeast, the intermediate gently WNW, and the least more steeply to the south (Fig. 2 and Table 2).

In the hinge, the same material line that suffered, according to the most-plausible hypothesis, the greatest early contraction (the line now plunging about 50° W) is

a line of considerable calculated late extension. This agrees with the tentative deformation history of the nodules; having taken part in only the latest strain phases, their shape axes form small angles with the corresponding axes of the calculated late matrix strain (Fig. 2). One may conclude that the strain history in the hinge was one of essentially coaxial increments.

In the limb, however, the W-plunging intermediate axes of early and late strain coincide only approximately, and the intermediate nodule axis is horizontal and forms a significant angle with both. That the least-strain and shortest nodule axes nearly coincide is not diagnostic because cleavage and bedding form such a small angle and the nodules may have started as oblate objects in the bedding plane. The calculated incremental maximum-strain axes do diverge strongly. The long 'early' strain axis plunges to the ESE, the 'late' to the northeast, and the nodule axis, probably marking the very latest strain increment, plunges steeply northward, down the cleavage dip (Fig. 2). The strain history of the limb was non-coaxial, hence probably one involving some flexural shear, and thus affected by rigid-body rotations.

The strongest evidence for systematic rigid-body rotation, indicative of a history of prolonged shearing, comes from the perturbations of the mean strain caused by the differential stiffness of nodules and matrix. The axes of the rigid-body rotations that are part of the perturbations (Appendix) are widely scattered in the hinge (Fig. 6c) but form a systematic pattern in the limb (Fig. 6f). The single cluster of axes has probably been caused by an average regimen of shearing, with an axis of rotation that remained approximately constant through time. If this regimen was locally perturbed by suspended stiff bodies, their vicinity must have caused retardations or accelerations of the rate of shear. The axes of local rotation with respect to the main body can thus be expected to parallel statistically those of the bulk rotation. The few perturbing rotation axes outside the main cluster, yet restricted to a narrow great-circle zone, may have been so restrained by the insignificance of internal strain in the material shear planes, making the probable strain history one of approximate simple shear.

In the hinge, with its more nearly coaxial strain history, perturbation rotation axes were not much constrained. The observed slight preference for vertical axes may have been caused by the transpression which has been recognized in the deformation history of the region (Soper & Hutton 1984, Soper 1986, 1988, Soper *et al.* 1987).

CONCLUSIONS

Rigid, calcareous, probably oblate-spheroidal concretions grew in soft, carbonate-rich muds soon after deposition and escaped the 40% volume loss of the compacting matrix. The mudstones formed a ductile member of a multilayer stack, between less ductile, graywacke-rich layers above and below. An early tectonic phase compressed the stack horizontally and perpendicularly to the later kinematic fold axis, shortening it by 9% at approximately constant volume, elongating it vertically, and leaving lines parallel to the future fold axis unchanged.

The rigid-body rotations necessary to bring beds to approximately their present orientation (apart from the minor internal rotations caused by strain) were probably spread over the deformation history. Most of the 87° buckling of the limb relative to the hinge probably occurred soon after the conclusion of the bedding-parallel contraction phase, but some of it may also have been concurrent with the late tectonic phase. The relative flexural displacement between competent layers that comes with buckling was partly taken up as simple shearing in the ductile interlayers (Chapple & Spang 1974), and in the limb the slate unit sandwiched between greywackes appears to have acted as such an interlayer. Local inhomogeneity of this flexural shear, especially next to the nodules, led to compatibility adjustments by relative rigid-body rotations, dominantly about the fold axis. Near the end of the deformation history, the matrix became stiffer and the calcarous nodules relatively less stiff (perhaps by a rise in temperature). Especially in the hinge region, the nodules have been strained most strongly in the latest stages of the tectonism.

Although cleavage consists mostly of spaced stress-solution folia, no internal contradictions arise if one assumes it to have tracked the plane normal to the direction of greatest shortening through a complex strain history (Oertel 1983) and uses the preferred orientation of phyllosilicate grains, inhomogeneous as it may be at the microscopic scale, for an estimate of the cumulative strain according to the geometric interpretations of March (1932). Rigid-body rotation, which distinguishes simple from pure shear, does not leave any physical evidence in a homogeneously deformed body; the presence of local perturbations of strain homogeneity, however, does furnish evidence for a history of simple shearing in the form of regularly oriented local rotation axes.

Acknowledgements—A. P. S. Reymer did the petrographic work for this research and took all the microphotographs. We thank the following: N. J. Soper led G. Oertel to the outcrop, R. T. Chen found and eliminated a mistake in the calculations, and Peter Bird, Ray Fletcher, Win Means, Jack Soper, Sue Treagus and John Wheeler improved and helped shorten the paper. Julie Guenther did the drafting, and Ram Alkaly prepared the hundreds of thick sections needed for this study. National Science Foundation grants GA 37100, EAR 76-04403, EAR 78-00847 and EAR 82-18039 supported the research.

REFERENCES

Bond, G. C. & Kominz, M. A. 1984. Construction of tectonic subsidence curves for the early Paleozoic miogeocline, southern Canadian Rocky Mountains: Implications for subsidence mechanisms, age of breakup, and crustal thinning. *Bull. geol. Soc. Am.* **95**, 155–173.

Chapple, W. M. 1969. Fold shape and rheology: The folding of an isolated viscous-plastic layer. *Tectonophysics* **7**, 97–116.

Chapple, W. M. & Spang, J. H. 1974. Significance of layer-parallel slip during folding of layered sedimentary rocks. *Bull. geol. Soc. Am.* **85**, 1523–1534.

Fletcher, R. C. & Pollard, D. D. 1981. Anticrack model for pressure solution surfaces. *Geology* **9**, 419–424.
March, A. 1932. Mathematische Theorie der Regelung nach der Korngestalt bei affiner Deformation. *Z. Kristallogr.* **81**, 285–297.
McCabe, P. J. 1972. The Wenlock and Lower Ludlow strata of the Austwick and Horton-in-Ribblesdale inlier of north-west Yorkshire. *Proc. Yorks. geol. Soc.* **39**, 167–174.
McCabe, P. J. & Waugh, B. 1973. Wenlock and Ludlow sedimentation in the Austwick and Horton-in-Ribblesdale inlier, north-west Yorkshire. *Proc. Yorks. geol. Soc.* **39**, 445–470.
Miller, D. M. & Oertel, G. 1979. Strain determination from the measurement of pebble shapes: a modification. *Tectonophysics* **55**, T11–T13.
Oertel, G. 1978. Strain determination from the measurement of pebble shapes. *Tectonophysics* **55**, T1–T7.
Oertel, G. 1981. Strain estimation from scattered observations in an inhomogeneously deformed domain of rocks. *Tectonophysics* **77**, 133–150.
Oertel, G. 1983. The relationship of strain and preferred orientation of phyllosilicate grains in rocks—a review. *Tectonophysics* **100**, 413–447.
Oertel, G. 1985a. Reorientation due to grain shape. In: *Preferred Orientation in Deformed Metals and Rocks: An Introduction to Modern Texture Analysis* (edited by Wenk, H.-R.). Academic Press, New York, 259–265.
Oertel, G. 1985b. Phyllosilicate textures in slates. In: *Preferred Orientation in Deformed Metals and Rocks: An Introduction to Modern Texture Analysis* (edited by Wenk, H.-R.). Academic Press, New York, 431–440.
Oertel, G., Engelder, T. & Evans, K. 1989. A comparison of the strain of crinoid columnals with that of the enclosing silty and shaly matrix on the Appalachian Plateau, New York. *J. Struct. Geol.* **11**, 975–993.
Ramsay, J. G. 1967. *Folding and Fracturing of Rocks*. McGraw-Hill, New York.
Soper, N. J. 1986. Geometry of transecting, anastomosing solution cleavage in transpression zones. *J. Struct. Geol.* **8**, 937–940.
Soper, N. J. 1988. Timing and geometry of collision, terrane accretion and sinistral strike-slip events in the British Caledonides. In: *The Caledonian–Appalachian Orogeny* (edited by Harris, A. L. & Fettes, D. J.). *Spec. Publs geol. Soc. Lond.* **38**, 481–492.
Soper, N. J. & Hutton, D. H. W. 1984. Late Caledonian sinistral displacements in Britain: implications for a three-plate model. *Tectonics* **3**, 781–794.
Soper, N. J., Webb, B. C. & Woodcock, N. H. 1987. Late Caledonian transpression in North West England: timing, geometry and geotectonic significance. *Proc. York. geol. Soc.* **46**, 175–192.
Wenk, H.-R. 1985. Measurement of pole figures. In: *Preferred Orientation in Deformed Metals and Rocks: An Introduction to Modern Texture Analysis* (edited by Wenk, H.-R.). Academic Press, New York, 11–47.
Wheeler, J. 1986. Average properties of ellipsoidal fabrics: Implications for two- and three-dimensional methods of strain analysis. *Tectonophysics* **126**, 259–270.

APPENDIX

(1) *Calculation of the pole of a material plane before a strain*

For a conventionally expressed finite strain, ε_{ij} (for diagonal components of this tensor, strain is the difference between final and original lengths divided by the original length), the stretch tensor is A_{ij}:

$$A_{ij} = \varepsilon_{ij} + \delta_{ij},$$

where δ_{ij} is the Kronecker delta or identity matrix. A_{ij}, acting as a transformation matrix, modifies undeformed position vectors X_i into their deformed counterparts x_i (both Cartesian co-ordinate systems, with common origin and orientation) as follows:

$$x_i = A_{ij}X_j,$$

(a subscript repeated in the same term implies summation over that subscript, say j, $j = 1$–3). Material lines V_i, if strained by ε_{ij}, become v_j by the transformation:

$$v_j = A_{ij}V_j.$$

Poles to material planes transform, except for a scale factor, as if they were material lines subject to the inverse of the strain. Hence, for a bedded rock in which the strain is ε_{ij} the pole to the unstrained bedding plane can be found by noting that the stretch A_{ij} for the observed strain is the inverse of that for unstraining. A vector p_i' parallel to the unstrained bedding pole thus is:

$$p_i' = A_{ij}p_j,$$

where p_j is the pole to the observed, strained bedding plane. (Note that this equation would produce the forward strain on the vector p_j if that vector represented a material line in the undeformed material.) To represent the unstrained pole by a conventional unit-vector, u_i, the vector p_i' must be normalized by division with its own magnitude:

$$u_i = p_i'/(p_i'p_i')^{1/2}.$$

This finding is the equivalent of Ramsay's (1967, pp. 129–134).

(2) *Calculation of a strain perturbation*

If we assume, arbitrarily, that each individual observed strain is the result of the action of the mean strain represented by the stretch tensor **M** (subscripts dropped for convenience) preceded by the local strain perturbation **S**, we postulate that a transformation matrix **T'** (composed of the locally observed stretch, **O**, and an earlier rotation **R'**) is related to the mean and perturbation stretch tensors by the equations:

$$\mathbf{OR'} = \mathbf{T'} = \mathbf{MS}.$$

Without having to determine either this transformation matrix or this rotation, we can also postulate the following:

$$\mathbf{T} = \mathbf{M}^{-1}\mathbf{O},$$

where **T** is another transformation matrix, the stretch portion of which is the perturbing stretch **S**. **T** can then be left-polar-decomposed (meaning that we assume that any rigid-body rotation represented by **T** has preceded the strain represented by **S**) to yield **S** in co-ordinates materially anchored in the sample. Decomposition proceeds as follows:

$$\mathbf{S} = [\mathbf{TT}^{\mathrm{T}}]^{1/2},$$

where $\mathbf{T}^{\mathrm{T}}$ is the transpose of **T** and the square root of the symmetric 'square' matrix in brackets is understood to mean the result of first diagonalizing this matrix by finding its eigenvalues and eigendirections, then taking the square roots of the eigenvalues, and finally restoring the new diagonal tensor to its original orientation by the eigendirection matrix. The result, **S**, is the stretch tensor of the strain perturbation. The rotation **R** (the inverse of **R'**) contained in the transformation matrix **T** is found by:

$$\mathbf{R} = \mathbf{S}^{-1}\mathbf{T}.$$

The temporal sequence, rotation first, strain perturbation second and mean strain last, is artificial, but the need for a relative rotation **R** between a domain subject only to the mean strain and another, continuous with the first but also affected by the strain perturbation, exists physically because of the necessity to satisfy the compatibility requirement.

(3) *Calculation of the 'late' strain*

This is another problem of strain factorization and polar decomposition. Assuming a common 'early' strain history for hinge and limb, we rotate the early stretch tensor so as to fit the unstrained domainal attitudes of bedding and fold axis. We further assume that the present mean stretch is the strain portion **M*** of a transformation matrix **M'** (asterisks for symmetric stretch tensors and primes for generally unsymmetric transformation matrices), which resulted from the sequential action of the 'early' stretch **E*** followed by the 'late' stretch **L***:

$$\mathbf{M}' = \mathbf{L}^*\mathbf{E}^*.$$

This argument can again be inverted, save for the unknown rotations:

$$\mathbf{L}'^{-1} = \mathbf{E}^*\mathbf{M}^{*-1}.$$

We solve for the inverse of the transformation matrix $\mathbf{L}'$ containing the 'late' stretch $\mathbf{L}^*$, by letting the inverse of the observed mean stretch be 'followed' by the forward 'early' stretch $\mathbf{E}^*$. The resulting transformation matrix $\mathbf{L}'^{-1}$ inverts to $\mathbf{L}'$, and the symmetric stretch $\mathbf{L}^*$, representing the strain portion of this matrix, is extracted by left-polar decomposition as in (2) of this Appendix. Left decomposition yields eigendirections of the 'late' strain with reference to co-ordinates anchored in material lines of the sample, because rotation is taken to have preceded the strain.